by U. Dürig

Atomic-scale metal adhesion investigated by scanning tunneling microscopy

The interaction of a sharply pointed metal tip with a metal surface is investigated both theoretically and experimentally. By resorting to an effective potential approach, the characteristics of tip-sample forces are analyzed systematically in terms of known theory of bulk metal adhesion. Experiments probing the short-range adhesion interaction by means of a combination of force gradient sensing with tunneling microscopy are described. It is found that the concepts based on adhesion at a macroscopic level are not generally applicable in describing the observed tip-sample force gradient characteristics. These characteristics can. however, be explained in a semiguantitative way using effective interactions determined from a cluster calculation. It is also shown that the chemical information obtained by probing short-range interactions can be used to identify adsorbates on metal surfaces.

1. Introduction

The study of interactions at surfaces has a long history, in particular with regard to the adhesion of macroscopic bodies, because of their obvious technological relevance. Long-range molecular attraction due to van der Waals (vdW) forces was the first surface interaction to be investigated systematically [1]. Accurate control of the distance between the interacting bodies was one of the major experimental challenges. Ultimately, resolution is limited by the intrinsic roughness of the surfaces. To circumvent this problem, Tabor and Winterton [2] used a pair of orthogonally crossed mica cylinders as a sample. This technique allowed vdW interactions to be studied at distances approaching \approx 1.5 nm [3]. The scheme was also successfully used to investigate solvation forces and adhesion in polymer layers [4, 5].

Among the first to perform quantitative measurements of the interaction between metal surfaces were Derjaguin et al. [6]. However, lack of precise knowledge of the interaction geometry rendered interpretation of the data difficult. In particular, no information on the adhesion at

•Copyright 1994 by International Business Machines Corporation. Copying in printed form for private use is permitted without payment of royalty provided that (1) each reproduction is done without alteration and (2) the Journal reference and IBM copyright notice are included on the first page. The title and abstract, but no other portions, of this paper may be copied or distributed royalty free without further permission by computer-based and other information-service systems. Permission to republish any other portion of this paper must be obtained from the Editor.

distances close to contact could be obtained, though this regime is technologically of great importance. Another approach was followed by Buckley [7]. Instead of studying long-range vdW interactions, he concentrated on investigating metal-metal contacts and their effects on adhesion and friction. In a seminal experiment, wetting of the apex of a field-emission tip upon touching a substrate surface was studied on an atomic scale by means of field ion microscopy.

Microcontact experiments provide another important tool for examining surface interactions [8]. The technique relies on measuring stress-strain characteristics of the joint formed by a sharply pointed stylus which is gently pressed against a flat sample. Results are analyzed in terms of macroscopic concepts based on elastic and plastic deformation theory [9]. A general problem with contact mechanics is that details of the atomic interaction cannot be assessed. Instead, the latter is globally accounted for by a phenomenological interface energy. Moreover, applicability of macroscopic continuum mechanics becomes questionable at a submicron scale.

With the exception of the field ion microscopy study, the experimental techniques discussed above do not provide direct information on atomic-scale phenomena. The development of scanning tunneling microscopy (STM) and related local probe techniques, in particular scanning force microscopy (SFM) [10], have paved the way for a new class of experiments. These techniques allow the gap width between a probe tip and a sample surface to be controlled on a subnanometer scale. Moreover, atomic resolution has been demonstrated with both STM and SFM. Consequently, interactions can be studied on a previously inaccessible scale. This opens up new dimensions in adhesion science and the closely related field of tribology, which has profited substantially from recent advances of experimental techniques [11, 12].

Spurred by STM, microcontact experiments have been extended to the nanometer regime [13], in which the number of atoms involved becomes small enough for molecular dynamics simulations to be performed [14]. These investigations provide valuable insight into nanometer-scale mechanics, a field that will require increased attention in the near future as the trend toward miniaturization continues at a rate of approximately one order of magnitude per decade. The ultimate goal is to manipulate individual molecules or atoms in order to build new, more complex artificial structures. Spectacular results have recently been obtained which demonstrate the feasibility of controlling the motion of individual atoms on single-crystal surfaces [15].

In this paper the physics of local interactions is examined in the light of our own experimental work. The theme of the experiments has been to characterize tip-sample interactions during normal metal-vacuum-metal

tunneling operation of the STM. For this, the tunneling current fulfills two purposes. It provides a convenient parameter for controlling the tip-sample distance, and it serves to sense deflections of a spring used for measuring the interaction [16]. The tip-sample distance can be adjusted down to atomic dimensions, thus enabling us to study short-range metallic adhesion interactions involving electron wave function overlap. Little is known experimentally about these short-range interactions, yet they are of fundamental importance for the understanding of adhesion on an atomic as well as a macroscopic scale. In practice, macroscopic bodies are never perfectly flat. A typical surface is corrugated, with myriads of atomic-scale protrusions. A single asperity is investigated in an STMbased experiment, thus providing an extreme realization of the macroscopic world. Moreover, a thorough understanding of atomic-scale adhesion is crucial for building novel structures by manipulating atoms or molecules.

The paper is organized as follows. In the first part, metal adhesion theory is briefly reviewed, and the characteristics of the interaction of a sharply pointed tip with a flat surface are investigated using an effective potential approach. The experimental part begins with an introduction to the technique used for studying tip-sample interactions. In a subsequent section, measurements of the tip-sample force gradient as a function of distance are presented and discussed. Finally, applications of force gradient sensing as an imaging tool for surface studies are shown.

2. Metal adhesion

The interaction between a metal tip and a metallic sample arises from the quantum-mechanical description of the Coulomb interaction of the conduction electrons. Two regimes are differentiated depending on the separation of the bodies. At large distances, their respective electron wave functions do not overlap. The interaction is then dominated by vdW forces. These forces originate from quantum-mechanical fluctuations of the electron gas, which in turn give rise to space- and time-modulated dipole moments. The spontaneous dipole moments of one body interact with their respective images induced in the other body, and vice versa. The leading term of this attractive interaction has a power law dependence on distance, and its exponent depends on geometry [5]. At a gap width of the order of 0.3 nm, the electron wave functions overlap appreciably, and electron exchange becomes important. As a consequence, attractive exchange-correlation interaction (termed short-range adhesion interaction) becomes dominant at short distances. The corresponding forces decay exponentially with a decay constant comparable to the screening length of the conduction electrons.

For the moment we consider the interaction between two parallel half-spaces separated by a distance s. We assume that s is measured with respect to the jellium edges of the interacting bodies. The leading terms of the adhesion energy per unit area, $W_{\rm ad}$, due to the nonretarded vdW interaction are given by the well-known Lifshitz formula [17]

$$W_{\rm ad}(s) = \frac{\hbar \bar{\omega}}{16\pi^2 s^2} \,, \tag{1}$$

where we use the abbreviation

$$\bar{\omega} = \int_{0}^{\infty} \frac{\varepsilon_{1}(i\xi) - 1}{\varepsilon_{1}(i\xi) + 1} \frac{\varepsilon_{2}(i\xi) - 1}{\varepsilon_{2}(i\xi) + 1} d\xi. \tag{2}$$

Equation (2) is integrated in the complex ω -plane along the imaginary axis, and $\varepsilon_{1,2}(\omega)$ denote the complex dielectric functions of the half-spaces. Dielectric properties of simple metals are described fairly well by a free-electron approximation. The Lifshitz frequency $\bar{\omega}$ can then be expressed in terms of the plasma frequencies ω_{p_1,p_2} of the two half-spaces [18],

$$\bar{\omega} = \frac{\sqrt{2}\pi}{4} \frac{\omega_{p1}\omega_{p2}}{\omega_{p1} + \omega_{p2}}.$$
 (3)

For simple metals, the order of magnitude of the vdW interaction is adequately represented by Equation (3). For transition metals, however, $\bar{\omega}$ is underestimated by a factor of approximately two, because additional dissipation channels due to interband transitions must be taken into account. Typical values of $\hbar\bar{\omega}$ for metallic elements are of the order of 10 eV (values for some specific elements are cited in [18]).

The Lifshitz expression, Equation (2), emerges from a local approximation of the dielectric function [19]. This approximation is well justified for insulating materials, for which the interaction can be thought of being a linear superposition of the interaction between individual atoms. For metals, however, the motion of electrons is strongly correlated, and thus screening effects cannot be neglected. The latter become important for evanescent electromagnetic (plasmon) modes with a component of the wave vector parallel to the surface that is of the order of the Fermi wave number or larger. Because of the rapid decay of the corresponding electromagnetic fields, nonlocal effects become appreciable at separations smaller than about 0.6 nm. The corresponding theory is rather elaborate. Numerical results have been obtained for simple metals such as aluminum in the regime of negligible electron exchange [20] (in fact, the problem of electron exchange was excluded from the calculation by making the work function arbitrarily large). As a result of the nonlocal screening effects, the vdW interaction becomes weaker

than the Lifshitz formula would suggest. In particular, the divergence at $s \rightarrow 0$ is eliminated.

For sufficiently small gap widths, i.e., $s \leq 0.3$ nm, electron wave functions overlap appreciably, making it necessary to consider exchange effects [21]. The coupling between the metals eventually becomes so strong that perturbative approaches can no longer be used. Therefore, self-consistent density functional formalism [22, 23] combined with pseudopotential methods [24] has been employed to calculate interaction energies. One of the problems with density functional theory is that a local approximation is used for the exchange-correlation functional. As a consequence, binding energies are typically overestimated, and interactions due to correlated electron excitations cannot be treated at all. This means that long-range vdW interactions are not within the scope of such calculations, and interaction potentials typically fall off exponentially.

Rose et al. [23] calculated the adhesion energy for simple metals using a self-consistent local density formalism and a jellium model. They discovered that the interaction energy as a function of interface separation, $W_{\rm ad}(s)$, is fairly accurately represented by the Rydberg function with two scaling parameters, namely the maximum of the adhesion energy per unit area $E_{\rm ad}$ and a length scale $\ell_{\rm sc}$ approximately equal to the Thomas–Fermi screening length,

$$W_{\rm ad}(s) = E_{\rm ad}(1 + s/\ell_{\rm so}) \exp(-s/\ell_{\rm so}). \tag{4}$$

The theory was extended in a semi-phenomenological way to include all metallic elements, whereby the quantities $E_{\rm ad}$ and $\ell_{\rm sc}$ are inferred from cohesive properties of the metals [25].

As a representative example, we show in Figure 1 the interaction potential for two Al half-spaces using the following parameters: $\hbar \bar{\omega} = 8.2 \text{ eV} [18], E_{ad} = 10 \text{ eV nm}^{-2}$ [23], and $\ell = 0.066$ nm [25]. The upper panel shows the various contributions to the adhesion energy on an expanded scale. The dotted curve (A) corresponds to the nonretarded Lifshitz vdW interaction [Equation (1)]. The dashed curve (B), taken from [20], represents the vdW interaction taking into account effects due to finite screening. The short-range metallic adhesion interaction [Equation (4)] is indicated by the solid curve (C). The Lifshitz expression is clearly inadequate to describe the vdW interaction for interface separations smaller than 0.6 nm. The crossover from the vdW to the short-range metallic-adhesion regime occurs at a separation of ≈0.3 nm. The overall interaction potential obtained by interpolating curves B and C is depicted in the lower panel. Most of the adhesion energy (about 95%) is due to short-range interactions.



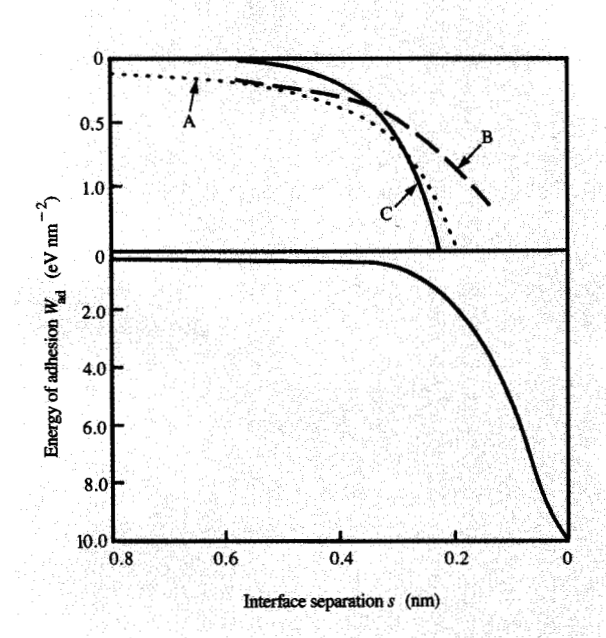


Figure 1

Adhesion energy of two Al half-spaces. Upper panel: curve A, van der Waals interaction, Lifshitz result; curve B, van der Waals interaction, Inglesfield result; curve C, short-range adhesion, Ferrante-Smith potential. Lower panel: Overall interaction potential obtained by interpolating curves B and C. (Adapted from U. Dürig and O. Züger, Proc. NATO ARW Nanosources and Manipulation of Atoms Under High Fields and Temperatures: Applications, V. T. Binh et al., Eds., Kluwer, Dordrecht, 1993, Vol. 235, pp. 271–286, reprinted with permission.)

3. Tip-sample interaction

In scanning probe microscopy one is concerned with the interaction of a sharply pointed probe tip with a substrate surface [Figure 2(a)]. This situation is substantially more complex than in the academic example of two interacting, ideally smooth half-spaces. As in electron tunneling, short-range forces are primarily sensitive to the atomic structure of the tip apex and the sample surface in a volume of atomic dimensions [Figure 2(b)]. VdW forces, on the other hand, probe a much larger volume and hence may contribute substantially to the overall interaction force although they are much weaker in strength. As a result, tip-sample interaction forces depend on the geometrical properties of the tip and sample involving length scales ranging over several orders of magnitude.

In order to gain at least some qualitative insight, we resort to an effective potential approach. Consider for the moment a tip consisting of atomic layers forming a pattern of parallel terraces interacting with a perfectly flat sample surface [Figure 2(d)]. The spacing between the atomic

layers d should be uniform. Let σ_i denote the cross section of the ith layer. To simplify matters, we regard each terrace as a subarea of an infinitely extended half-space. Hence, effects due to the finite size of the terraces and the influence of the steps are ignored. This is equivalent to the assumption that many-body effects for edge atoms are the same as those for atoms at the perfectly flat macroscopic surface. The tip-sample force may then be expressed as

$$F_{TS}(s) = \sum_{i=1}^{\infty} (\sigma_i - \sigma_{i-1}) F_{ad}[s + (i-1)d], \qquad (5)$$

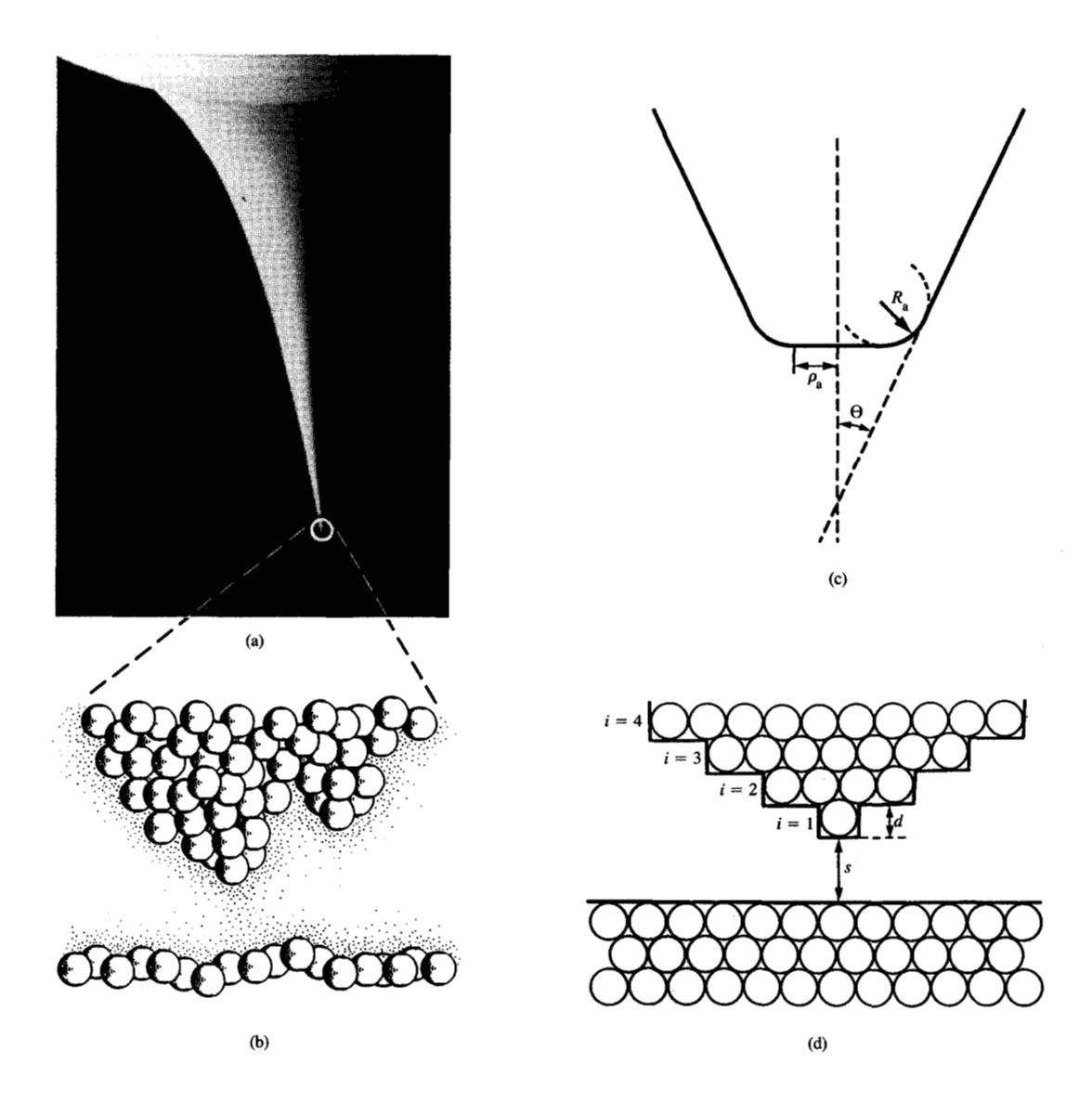
where $F_{\rm ad}=-dW_{\rm ad}/ds$ denotes the interaction force per unit area of two half-spaces (note that $\sigma_0\equiv 0$). In the spirit of the jellium model, the atomic structure is disregarded in a next simplification step. Accordingly, the discrete sum becomes an integral. By applying a partial integration transformation, one obtains

$$F_{TS}(s) = -\frac{dW_{ad}(s)}{ds} \sigma(0) + W_{ad}(s) \frac{d\sigma}{dz} (0)$$
$$+ \int_0^\infty W_{ad}(s+z) \frac{d^2\sigma}{dz^2} dz. \tag{6}$$

The tip-sample interaction is thus determined by the shape of the tip apex expressed by its cross section, σ_0 , and its radius of curvature, $R_a \equiv d\sigma/2\pi dz$, plus a correction term which takes into account the contributions of the tip shaft. In passing we note that the second term in Equation (6) corresponds to the so-called Derjaguin approximation. ¹

Equation (6) can be used to examine the influence of the tip geometry on the force-distance characteristics. First, we investigate the vdW interaction. Using the Lifshitz expression [Equation (1)] for W_{ad} , one immediately finds that the first, second, and third terms of Equation (6) scale as $1/s^3$, $1/s^2$, and 1/s, respectively. Hence, a hierarchy is introduced with respect to distance as a direct consequence of the power law dependence of the vdW interaction. The surface of a real tip is corrugated. Therefore, it is not immediately clear how to evaluate the tip parameters in Equation (6) in a meaningful way. Clearly, atomic-scale roughness plays only a minor role, if any. Hence, one is inclined to use some smoothing procedure to evaluate effective tip parameters. This point is addressed in more detail below. For the time being, let us assume that the actual tip can be represented by an effective tip, as shown in Figure 2(c). The apex is formed by a flat terrace having a radius ρ_a . The terrace connects smoothly to a conical shaft with an opening angle Θ , and the transition zone is characterized by a radius of curvature R_a . At short distances, $s \leq \rho_a^2/R_a$, the inverse

¹ See [5], Chapter 10.



Tip-sample interaction forces depend on the geometrical properties of the tip involving length scales ranging over several orders of magnitude. (a) Long-range van der Waals forces probe the structure of the tip on a scale comparable to the tip-sample distance. [Courtesy of O. Albrektsen et al., submitted to J. Vac. Sci. Technol. B (1994), reprinted with permission.] (b) Short-range adhesion forces involving electron wave function overlap are sensitive to the atomic structure of the very apex of the tip. [From G. K. Binnig and H. Rohrer, Les Prix Nobel (©The Nobel Foundation, Stockholm, 1987), pp. 85–111, reprinted with permission.] (c) Effective tip-shape characterized by the radius of the apex, ρ_a , the radius of curvature at the apex, R_a , and the opening angle, Θ , of the conical shaft. (d) Idealized representation of the tip apex as a series of close-packed parallel terraces.

cubic term dominates. Then the inverse quadratic term takes over up to a distance of $s = R_a/\tan^2 \Theta$. Finally, the interaction force slowly falls off at a rate of 1/s (as long as retardation effects can be neglected, i.e., if $s \leq 10$ nm). In the regime of the fully retarded vdW interaction,

 $s \ge 100$ nm, this term would fall off at a rate of $1/s^2$. In the transition regime the exponent varies smoothly from -1 to -2.

The situation is different for the short-range interaction. Owing to the exponential cutoff, the integral term has a less dramatic effect. By using the Ferrante-Smith potential [Equation (4)] and applying partial integration transformations, one finds

$$F_{\text{TS}}(\tilde{s}) = E_{\text{ad}} \ell_{\text{sc}} \exp(-\tilde{s}) (\bar{M}_0 - \bar{M}_1 - \tilde{s}\bar{M}_0)$$
 (7a)

with

$$\widetilde{M}_{n} = \int_{0}^{\infty} \widetilde{\sigma}(\widetilde{z})\widetilde{z}^{n} \exp(-\widetilde{z}) d\widetilde{z} \qquad n = 0, 1, \tag{7b}$$

where linear dimensions are scaled with $\ell_{\rm sc}$ (the tilde denotes scaled variables), and \overline{M}_0 and \overline{M}_1 are the zeroth and first moments of the exponentially weighted tip cross section. The structure of Equation (7a) is similar to that of the interaction potential; i.e., it consists of an exponential factor and a linear term, the latter containing all the geometrical information.

Defining an effective tip shape is straightforward for the short-range Ferrante-Smith adhesion potential. Inspection of Equations (7) reveals that the tip-sample force can be represented as a superposition of the adhesion potential and its derivative. Hence, by comparison with Equation (6) one can define an effective apex radius and an effective radius of curvature at the apex, respectively, as follows:

$$\begin{split} &\rho_{\rm a}=\,\ell_{\rm sc}\,\sqrt{\frac{2\tilde{M}_0-\tilde{M}_1}{\pi}}\,,\\ &R_{\rm a}=\,\ell_{\rm sc}\,\frac{\tilde{M}_1-\tilde{M}_0}{2\pi}\,. \end{split} \tag{8}$$

Two parameters are thus sufficient to describe the tip-sample force. By virtue of the above transformation the integral term can be made to vanish, a fact that reconciles the sensitivity of the short-range adhesion interaction to the shape of the very apex of the tip.

The problem of tip roughness is now investigated from a more general perspective. Let us assume that the roughness has a finite correlation length. Hence, the concept of a scale-invariant mean tip shape can be used. The integral representation of Equation (5) serves as a starting point. The tip-sample interaction is thus given by the convolution product of the derivative of the tip cross section with respect to the sample surface normal and the interaction force per unit area of two half-spaces. Let h(z) be a symmetric, normalized smoothing function. We define the smoothed-tip cross section $\bar{\sigma}(z)$ as the convolution product of the smoothing function with the tip cross section. With this definition, we obtain the following for the interaction force of the smoothed tip with a flat sample:

$$\overline{F_{TS}}(s) = \int_0^\infty \frac{d\overline{\sigma}(z)}{dz} F_{ad}(s+z)$$

$$= \int_0^\infty \frac{d\sigma(z)}{dz} F_{ad}(s+z) dz$$

$$+ \frac{1}{2} \int_0^\infty \frac{d\sigma(z)}{dz} M^{(2)}(h) \frac{d^2 F_{ad}(s+z)}{dz^2} dz$$

$$= F_{TS}(s) + \Delta F_{TS}(s, h), \tag{9}$$

where $M^{(2)}(h)$ denotes the second moment of the smoothing function. Thus, the difference $\Delta F_{TS}(s,h)$ between the tip-sample force of the smoothed tip and the true tip is imperceptible if the condition

$$\left| \frac{1}{2} \frac{d^2 F_{ad}(s+z)}{dz^2} M^{(2)}(h) \right| \ll |F_{ad}(s+z)| \tag{10}$$

holds. In other words, the width of the filter function must be smaller than the square root of the absolute value of the adhesion force divided by its second derivative with respect to interface separation. If the Ferrante-Smith potential is substituted, a maximum width of the filter function of the order of the decay constant of the interaction, ℓ_{so} , is obtained irrespective of the tip-sample distance. For short-range adhesion interaction, atomicscale features are thus important even at large distances! Conversely, for vdW interaction the maximum width of the filter depends on the tip-sample distance. Substituting the Lifshitz potential into Equation (10), one finds that the width over which the tip cross section may be averaged is of the order of $s/\sqrt{3}$. Thus, the details of the tip shape are of less concern the farther away it is from the surface.

Short-range forces are sensitive to the atomic structure even at large distances. On the other hand, one cannot expect to be able to detect these interactions at distances larger than a few tenths of a nanometer, as they are eventually buried in a much larger background because of vdW interactions. The question now remains as to which of the two interactions is dominant. To obtain some quantitative understanding of this question, the interaction of the microtip depicted in Figure 2(d) with a flat surface is investigated first. The interaction potential is the same as that considered in Figure 1, and Equation (5) is used to calculate the tip-sample force. The result of the calculation is shown in Figure 3(a). The dotted curve corresponds to the short-range adhesion interaction. The dashed curve is obtained if the vdW interaction is included. The latter has little effect on the interaction of the microtip with the substrate, as expected. Note also that the magnitude of the tip-sample force is determined primarily by the size of the terrace at the very apex of the tip.

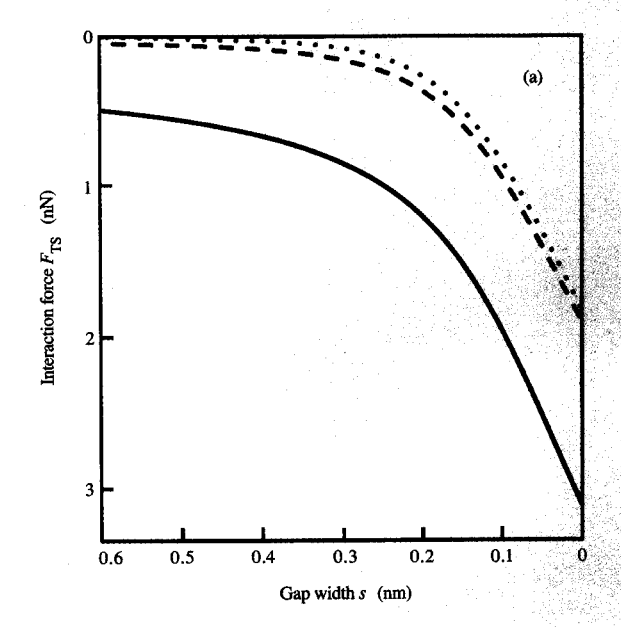
 $^{^{2}}$ The result is readily obtained by commuting the ordering of the convolution products and by using a second-order Taylor expansion of the interaction force $F_{\mathrm{TS}}(z)$.

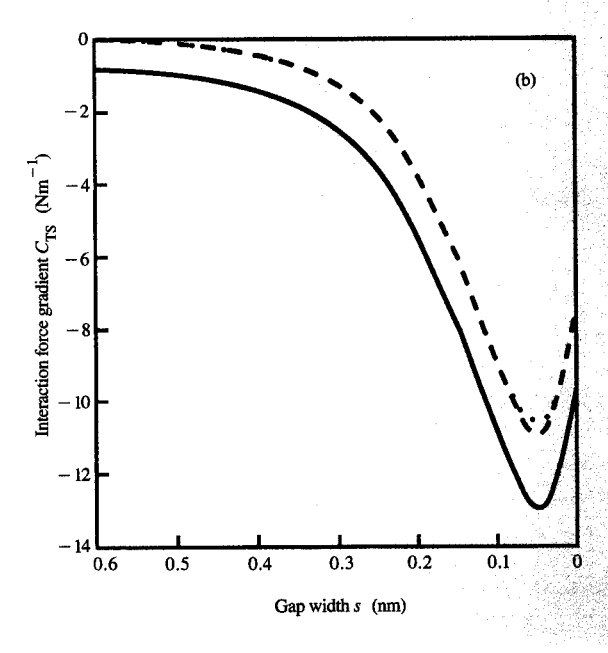
In reality, an isolated microtip does not exist. The closest realization would be a pyramidal single-atom fieldemitter tip [26]. More likely, however, the mean shape of the tip apex is spherical, with many microtip-like protrusions. The microtip that comes closest to the surface determines the tunneling current and the short-range adhesion interaction; the respective contributions of the other microtips may be neglected. The exact structure of the tip apex plays a minor role in the vdW interaction. If one assumes that the roughness has a mean height of 1 nm, this corresponds to a height variation of five atomic layers. In accordance with Equation (10), a width of the smoothing function of the same order of magnitude can be employed, thus eliminating the atomic-scale corrugation almost completely. Therefore, the support is represented as a smooth sphere, assuming an ad hoc value of $R_{\circ} = 10$ nm for the radius. Since the tip-sample distances considered here are small compared to R_a , the second term in Equation (6) provides a valid approximation for the calculation of the vdW force. The solid curve in Figure 3(a) represents the total tip-sample interaction including the contribution from the support. The latter is substantial but does not change appreciably with distance. This property is independent of the particular choice of R_a . Hence, the shape of the adhesion force curve at short distances is determined by the atomic structure of the tip apex and short-range adhesion forces, whereas the net attractive force measured at a distance larger than =0.5 nm provides information on the overall shape of the apex. Accordingly, the interaction force gradient [Figure 3(b)] is only marginally influenced by vdW forces. Therefore, by measuring interaction force gradients, one is able to enhance the sensitivity to short-range interactions substantially, a fact that is exploited in the present experiments.

The discussion of tip-sample interaction has been restricted to short-range adhesion and vdW forces, which are the important effects at a tunneling distance. In addition, Coulomb interactions arising from surface charges must be considered at larger tip-sample separations. Surface charges originate 1) from applying an external potential, 2) from work function differences of the probing tip and the sample, and 3) from local variations of the work function on the surfaces of the two bodies [27]. If tip and sample are ferromagnetic, magnetostatic forces are present and can be exploited for high-resolution domain imaging [28].

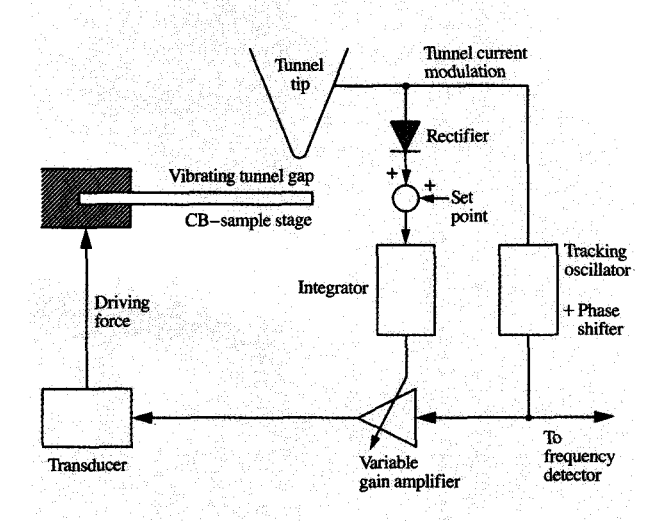
d Force sensors

Tip-sample interaction forces are sensed by means of a spring to which either the tip or the sample is attached. The physical concepts can be readily explained by





(a) Interaction force and (b) force gradient for a tip consisting of a microtip asperity like the one shown in Figure 2(d) on a spherical support with a radius $R_{\rm a}$ of 10 nm. Dotted and dashed lines correspond respectively to the short-range adhesion and the van der Waals interaction of the isolated microtip with a flat sample. The total tip-sample interaction including the support is represented by the solid line. (Adapted from U. Dürig and O. Züger, Proc. NATO ARW Nanosources and Manipulation of Atoms Under High Fields and Temperatures: Applications, V. T. Binh et al., Eds., Kluwer, Dordrecht, 1993, Vol. 235, pp. 271–286, reprinted with permission.)



Mark Trans

Schematic diagram of the setup used for measuring tip-sample interaction force gradients. (From [29], reprinted with permission.)

representing the spring as a harmonic oscillator with one degree of freedom. Accordingly, the sensor is characterized by a spring constant C and a resonance frequency ω_0 . The interaction between tip and sample is described by a potential $U_{\rm TS}(z)$, where z is an experimentally defined measure for the separation of the bodies. Note that experimental situations exist in which the premise of potential forces does not apply, e.g., because of viscous drag effects. The latter is most likely the case if experiments are conducted at ambient conditions or in liquid environments.

The entire system is fully described by its Hamiltonian,

$$H = \frac{C}{2} \left(\frac{p^2}{\omega_0^2} + y^2 \right) + U_{TS}(z), \tag{11}$$

and the corresponding partition function (the terms y and p denote the spring deflection and the conjugate momentum, respectively). At sufficiently low temperatures (which are specified below), the thermodynamic expectation value of the spring deflection $\langle y \rangle$ is equivalent to the condition of classical force balance, $Cy_0 - dU_{TS}/dz = 0$, where y_0 denotes the spring deflection in the absence of thermal vibrations.

Because of thermal agitation, the spring fluctuates around its mean value. Expansion of the Hamiltonian in terms of these fluctuations, $\Delta y \equiv y - \langle y \rangle$, yields

$$H - H(y_0) = \frac{C_{\text{eff}}}{2} \left(\frac{p^2}{\omega_0^2 C_{\text{eff}}/C} + \Delta y^2 \right)$$

$$+ \frac{C_{\text{eff}}}{2} (\langle y \rangle - y_0)^2 + \Delta y C_{\text{eff}} (\langle y \rangle - y_0)$$

$$+ \sum_{n=3} \Delta y^n \frac{d^n U_{\text{TS}}(z)}{n! dz^n} , \qquad (12a)$$

with

$$C_{\text{eff}} = C + \frac{d^2 U_{\text{TS}}}{dz^2} \,. \tag{12b}$$

The first term in Equation (12a) corresponds to a harmonic oscillator with a shifted resonance frequency ω_r determined by the resonance frequency of the unperturbed spring and the interaction force gradient $C_{TS} \equiv d^2 U_{TS}/dz^2$:

$$\omega_{\rm r} = \omega_0 \sqrt{1 + \frac{C_{\rm TS}}{C}} \,. \tag{13}$$

Note that the system is stable against fluctuations only if the effective spring constant is greater than zero. This implies that the stiffness of the spring cannot be made arbitrarily small when one is sensing attractive interactions for which the force gradient is negative. The other terms in Equation (12a) describe anharmonic corrections arising from higher-order terms of the interaction potential. The latter become noticeable for large vibration amplitudes Δy . As a consequence, the equilibrium spring deflection $\langle y \rangle$ and the point of classical force balance y_0 are no longer identical. As long as their difference is small compared to the vibration amplitude, anharmonic corrections are of minor importance. The order of magnitude of the effect can easily be estimated, because at the minimum of the free energy the corresponding terms in Equation (12a) approximately cancel. Hence, one concludes that anharmonicity may be neglected if

$$1 \gtrsim \frac{1}{C_{\text{eff}}} \sum_{n=3} \Delta y^{n-2} \frac{d^n U_{\text{TS}}(z)}{n! \ dz^n} \simeq \frac{\Delta y}{6C_{\text{eff}}} \frac{d^3 U_{\text{TS}}(z)}{dz^3} \ . \tag{14}$$

Two independent modes of operation of the force sensor are conceivable. In a static mode, the interaction force is determined by measuring the spring deflection $\langle y \rangle$. This mode requires accurate length measurements. The dynamic mode, on the other hand, provides information on the force gradient from a frequency measurement, a fact that simplifies quantitative experiments considerably. Therefore, and also because force gradient measurements are particularly well suited for investigating short-range adhesion interactions, all of our experiments were performed in the dynamic mode.

In our experiments, a flexible cantilever beam (CB) serves simultaneously as a spring and sample stage in a

normal STM (Figure 4). Interpretation of measured frequency shifts is straightforward because the dynamics of the first eigenmode of the CB is well represented by a simple spring model using a resonance frequency and spring constant that are identical to those of the CB [29]. Vibrations of the CB are detected by means of the tunneling current, which also serves as a control parameter of the tip-sample distance.

Thermal noise and external feedback provide the driving force for the CB vibrations. Without external feedback, the CB vibrates pseudoperiodically with a mean amplitude of $\Delta y = k_{\rm B} T/C_{\rm eff}$ as prescribed by the equipartition theorem. The frequency spectrum of the fluctuations is proportional to the frequency response of a spring resonator, which is a Lorentzian with a width $\omega_{\rm r}$ divided by the Q-factor of the resonance. The width of the frequency spectrum reflects the fact that the phase and the amplitude fluctuate with time. In principle, amplitude fluctuations have no effect on the frequency measurement, but phase fluctuations limit its accuracy. The mean square frequency fluctuation due to random thermal phase noise increases with the detection bandwidth BW and is inversely proportional to the Q-factor [29]

$$\Delta\omega_{r}^{2} = \omega_{r}BW/2Q. \tag{15}$$

The sensitivity of the frequency measurement is substantially increased by coherently exciting the spring by means of a linear feedback amplifier. As a result of the feedback, the apparent Q-factor increases in proportion to the energy stored in the resonator scaled by the thermal energy. Thus, the accuracy of the frequency measurement improves with the vibration amplitude of the resonator. By using Equations (13) and (15) and expressing the energy in the resonator in terms of its vibration amplitude, one obtains for the mean square fluctuation of the force gradient measurement

$$\Delta C_{\rm TS}^2 \simeq \frac{BWk_{\rm B}TC}{\omega_0 2Q\Delta y^2} \,. \tag{16}$$

In practice, an upper limit for the vibration amplitude is imposed by the nonharmonic terms of the interaction potential. Equation (14) can be used to estimate the maximum tolerable vibration amplitude in our experiments which entail the measurement of short-range adhesion interactions. Accordingly, rather stiff beams with a spring constant of the order of C=100 N/m are employed for the sake of stability. The tip-sample interaction is approximated by the Derjaguin term using a radius of R=0.15 nm to represent a tip apex of atomic dimensions, and by the Ferrante-Smith potential with values of $E_{\rm ad}=20~{\rm eV\, nm}^{-2}$ and $\ell_{\rm sc}=0.05$ nm for the energy of adhesion and the length scale, respectively. Thus, one obtains for the maximum tolerable vibration amplitude

 $\Delta y_{\rm max} \simeq (C\ell_{\rm sc}^2)/(RE_{\rm ad})$ a value of 0.05 nm, which is only eight times larger than the intrinsic thermal vibration! Typical Q-factors of the CBs are of the order of 200 to 400. Therefore, the detection threshold for measuring interaction force gradients is of the order of 1 Nm⁻¹ times the square root of the normalized detection bandwidth BW/ω_s .

For the feedback method to be useful, it must be possible to adjust the feedback gain in order to maintain a constant vibration amplitude. Furthermore, the oscillation frequency of the excited resonator must be identical to its resonance frequency. Unfortunately, this condition is not generally fulfilled, unless the driving force and the vibration of the resonator are exactly 90° out of phase [29]. The setup of the oscillator circuit used in the present experiments is shown in Figure 4 [29, 30]. A piezoelectric transducer converts an electrical signal into a driving force that excites the CB vibrations. They in turn give rise to a modulation of the tunneling gap and hence also of the tunneling current (it is assumed that the resonance frequency of the CB is higher than the cutoff frequency of the control loop which adjusts the tunneling gap). A tracking oscillator is used to lock in on the main frequency component of the tunneling current modulation. The same oscillator also serves as a phase-locked loop frequency detector for measuring the resonance frequency of the CB. A variable phase shifter allows one to adjust the phase of the oscillator signal with respect to the tunneling current response in order to compensate for propagation delays of the piezoelectric transducer and the tunneling current measuring electronics. Thus, the proper phase relation can be established, yielding accurate tracking of the resonance frequency. The amplitude of the tracking oscillator signal is controlled by means of a variable gain amplifier which in turn is connected to the piezoelectric transducer. When the gain of the amplifier is increased, oscillation sets in spontaneously. By adjusting the gain accordingly, a constant vibration amplitude is maintained. This task is performed by a second feedback circuit consisting of a rectifier for measuring the amplitude of the tunneling current modulation and an integrator to control the gain of the amplifier. An important feature of the circuit is that the gain can assume positive as well as negative values depending on whether the vibration amplitude is respectively smaller or larger than the set point. In the first case, the relative phase between excitation and response of the CB is such that its vibrational energy increases. In the second case, the phase is reversed; hence, vibrational energy is dissipated. The latter property is extremely important, because relaxation times would be prohibitively long without additional selective damping.

5. Force gradient characteristics

According to macroscopic adhesion theory, the tip-sample interaction force gradient measured as a function of

355

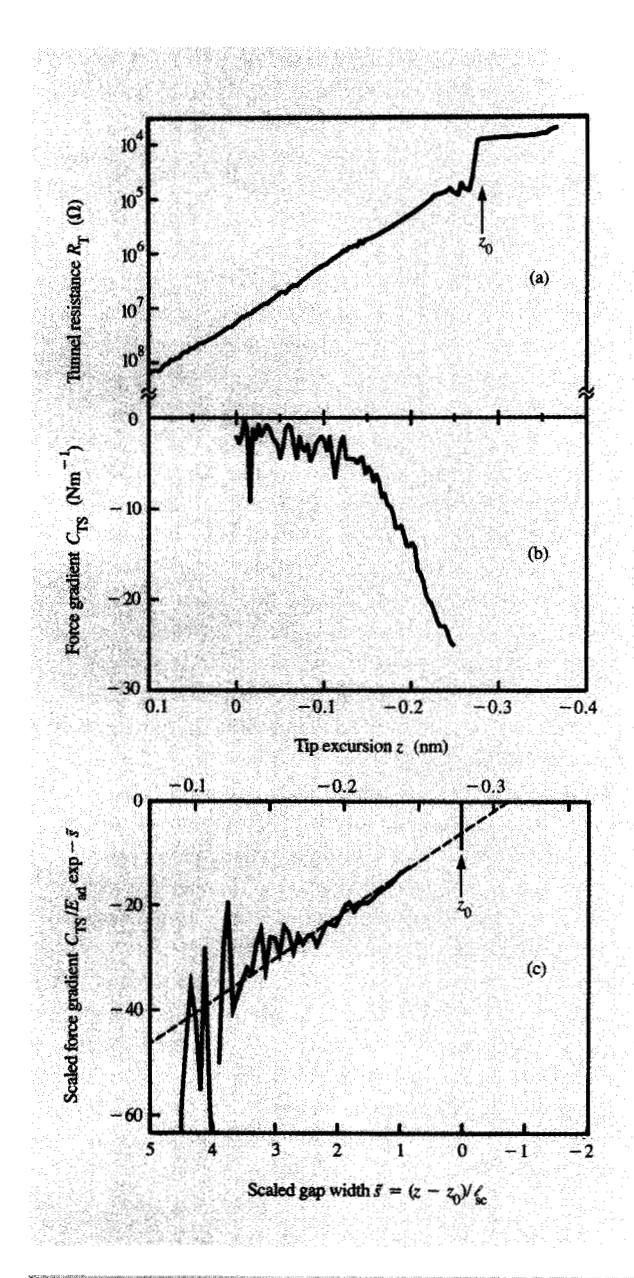


Figure 4

(a) Tunneling resistance and (b) interaction force gradient measured as a function of tip excursion using an Ir tip above an Ir sample. (c) Plot of the interaction force gradient normalized by $E_{\rm ad} \exp[-(z-z_0)/\zeta_0]$ using $E_{\rm ad} = 30$ eV nm⁻², $\zeta_{\rm c} = 0.042$ nm, and $z_0 = -0.27$ nm. (Adapted from [32] and reprinted with permission.)

distance should follow a universal law. This prediction is also supported by a more refined calculation by Banerjea et al. based on equivalent crystal theory [31]. The first experimental check was performed using Ir for the tip and as sample material [32]. This particular choice was made because Ir is chemically inert and the crystal lattice is

extremely rigid, as reflected by the high value of the elastic modulus. Tip and sample surfaces thus remain stable even at a gap width of less than 0.1 nm.

Experiments were conducted under ultrahigh vacuum conditions ($p \le 3 \times 10^{-10}$ mbar). Tunneling tips were made of mechanically sharpened Ir wire, and final tip forming was performed in situ. For this purpose a positive bias is applied to the tip using a constant current source. The current is set to 10 μ A, and the maximum tip voltage is limited to 800 V. The tip is first brought into contact with an Ir test sample. Then the tip is continuously retracted such that a constant gap voltage of ~700 V is obtained. The process is stopped when a steady state is reached. Quite frequently, tunneling images exhibit poor resolution after this treatment. Resolution is routinely enhanced, however, by applying a short positive voltage pulse of the order of 100 V to the tip while tunneling on the Ir test sample. The tip-forming procedure is crucial for obtaining reproducible force gradient measurements which are extremely sensitive to contamination. Without this treatment we have frequently observed large and positive interaction force gradients indicating the presence of repulsive forces even for tips that performed well in the tunneling microscope. Ir samples are prepared by extensively sputter-cleaning the surface of CBs made of polycrystalline Ir sheet metal. Typical values of the length, width, and thickness of the beams are 5 mm, 0.5 mm, and 50 μ m, respectively, yielding a resonance frequency of ≈1.5 kHz. The spring constant—typically of the order of 100 Nm⁻¹—is adjusted by positioning the tip between the clamped and the free ends of the CB, which has a nominal spring constant of $\approx 50 \text{ Nm}^{-1}$.

The interaction force gradient is measured as a function of the tip-sample distance z at a fixed position on the sample. Because z cannot be determined unambiguously, we define it as the displacement of the tip with respect to a reference position characterized by a specific value of the tunnel resistance; i.e., $R_{\rm T} = 10^7 \,\Omega$, corresponding to a tunneling current of 1 nA at a tunneling voltage of 10 mV. With the tip at the reference position, the feedback loop which adjusts for a constant tunneling current is interrupted, and the tip is ramped toward the CB surface at a rate of ≈ 0.1 nm s⁻¹. Thus, tunneling is used to establish a well-defined initial tip-sample distance for the approach experiments. The tunneling current and the resonance frequency are simultaneously recorded during approach. To prevent accidental touching of the surface, the tip is rapidly retracted to the reference position as soon as the tunnel resistance drops below $\approx 100 \text{ k}\Omega$. By this means, the tip is prevented from touching the surface. After each approach cycle, the feedback loop is turned on for 100 ms to compensate for possible drifts.

The result of such a measurement is shown in **Figure 5**. The force gradient and tunneling current curves represent

averages of 64 approach cycles. The interaction force gradient measured on the Ir sample is negative and increases rapidly in magnitude as z approaches -0.25 nm, which is the maximum tip excursion allowed by the tunnel resistance constraint. In a second experiment, the tunnel resistance limit was ignored in order to probe the contact regime. Here the tip eventually touches the sample surface, and, as a consequence, the atomic structure of the tip apex and the sample surface are irreversibly modified. Therefore, in contrast to the previous experiment, the data obtained in the individual approach cycles are not exactly identical. Hence, the continuation of the tunnel resistance curve for z < -0.25 nm is taken from a representative example of the second experiment. Typically, the tunnel resistance was observed to drop by one order of magnitude at $z \approx -0.27 (-0.05 + 0.02)$ nm, and it subsequently leveled off at $\approx 10 \text{ k}\Omega$. However, we were not able to reliably measure interaction force gradients in this regime.

The concept of tip-sample distance must be clarified before experimental data can be compared with theoretical predictions. The problem arises because there is no experimental measure for the width of the gap between tip and sample other than the tunneling current. The latter is influenced by too many unknown parameters which make it impossible to derive a reliable distance scale. The quantity that is readily amenable to experiment is the distance between the supports of the tip and sample. This distance is equivalent to the gap width up to an unknown, but constant, offset if relaxation is neglected. In the presence of relaxation, that same distance no longer translates linearly into a gap width. However, it still provides a linear measure for the distance between two hypothetical planes in the tip and sample, respectively, that are sufficiently far from the interaction zone for distortions of the atomic lattices to be negligible. Hence, comparison of experimental results with theoretical predictions is greatly facilitated if the latter specify the tip-sample separation relative to such reference planes.

In light of these facts, let us analyze the experimental tip excursion scale critically. First, the deflection of the CB is actually part of the sample deformation and hence should be accounted for. The deflection is so small (of the order of 0.01 nm at most; integration of the force gradient curves yields forces of the order of nanonewtons) that it can be neglected for the purpose of the experiment. Second, the tip excursion is measured with reference to a tip-sample distance specified by a particular value of the tunnel resistance. Although the tunneling current cannot be used as a scale for the gap width, it still provides a valid reference point for the tip excursion as long as the atomic structure of the tip does not change in the course of the approach experiment. This is ensured by the experimental procedure, which stops the ramp before irreversible modifications of the tip occur. Within these limits, the tip

excursion scale is thus a valid measure for the tip-sample separation in the sense stated above.

The distance dependence of the tip-sample force due to short-range adhesion contains an exponential term that reflects the chemical nature of the interaction and a linear term that contains the geometrical information [see Equation (7)]. The same general structure is also preserved for the force gradient

$$C_{TS} = E_{ad} \exp(-\tilde{s})(2\bar{M}_0 - \tilde{M}_1 - \tilde{s}\tilde{M}_0), \tag{17}$$

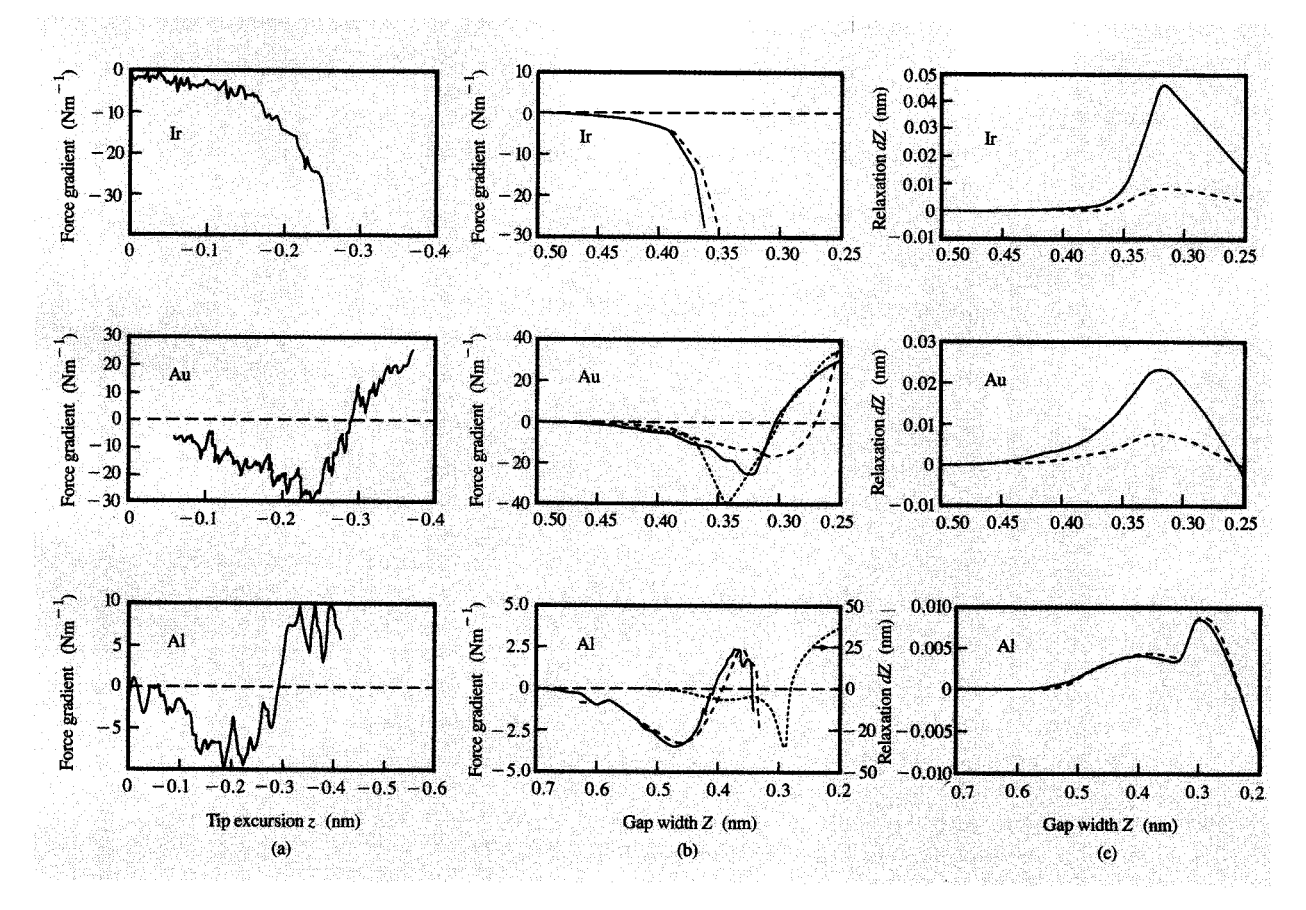
where the parameters $\tilde{M}_{0.1}$ are defined in Equation (7b). In order to compare the experimental results with the theoretical prediction, the tip excursion is scaled using the transformation $\tilde{s} = (z - z_0)/\ell_{sc}$. Values of 0.042 nm [25] and 30 eV nm⁻² [33] are substituted for the decay length $\ell_{\rm sc}$ and the maximum adhesion energy $E_{\rm ad}$, respectively. The offset parameter z_0 corresponds to the point where the jellium edges of the tip and sample touch. The position of the discontinuity of the tunnel conductivity at z = -0.27 nm can be identified as contact [34], and thus provides a reasonable ad hoc value for z_0 . A plot of the interaction force gradient divided by $E_{ad} \exp(-\tilde{s})$ should yield a straight line, and the tip parameters \tilde{M}_0 and \tilde{M}_1 can be calculated from the slope and the intersection of the line with the \tilde{s} -axis using Equation (17). Such a plot of the experimental data is shown in Figure 5(c). From a line fit one obtains $\tilde{M}_0 = 8.0$ and $\tilde{M}_1 = 21$, which yields an imaginary apex radius ρ_s [see Equation (8)]. This is readily corrected by selecting a different offset parameter z'_0 . The respective tip moments then transform as follows:

$$\widetilde{M}_0(z_0') = \exp(\widetilde{z}_0 - \widetilde{z}_0')\widetilde{M}_0(z_0)$$
(18)

and

$$\tilde{M}_{1}(z_{0}') = \exp(\tilde{z}_{0} - \tilde{z}_{0}') \left[\tilde{M}_{1}(z_{0}) - (\tilde{z}_{0} - \tilde{z}_{0}') \tilde{M}_{0}(z_{0}) \right]. \tag{19}$$

The requirements that ρ_a be real and R_a be positive yield $z_0 \le -0.295$ nm and $z_0 \ge -0.34$ nm, respectively. Thus the force gradient data allow us to specify the value of the offset parameter rather accurately without making a priori assumptions about the shape of the tip. Having specified z_0 , one can actually calculate the effective tip parameters which range from $\rho_a = 0/R_a = 0.1$ nm to $\rho_a = 0.15 \text{ nm/}R_a = 0 \text{ for } z_0 = -0.295 \text{ nm and}$ $z_0 = -0.34$ nm, respectively. Thus, the interaction seen in the experiment arises essentially from a single atom at the very apex of the tip. It is interesting to note that the conductivity jumps slightly before the hypothetically rigid tip would touch the surface. This indicates that the tip becomes stretched as it yields to the strong adhesion interaction, and, correspondingly, that the actual gap between the apex of the tip and sample surface closes more rapidly than for rigid bodies. The amount of relaxation estimated from the data is of the order of 0.05 nm.



Emma 8

Interaction force gradient characteristics for an Ir tip above Ir, Au, and Al substrates. (a) Experimental results. (b) Calculated using effective nearest-neighbor interactions: Dashed and solid lines correspond to the interaction of an Ir tip with a single substrate atom at the apex neglecting and including relaxation, respectively. Dotted lines correspond to the interaction of a pure Ir tip (note the change in scale for the Al substrate). (c) Tip (solid lines) and substrate (dashed lines) relaxations for the Ir–Ir, Ir(Au)–Au, and the Ir(Al)–Al systems. (Adapted from [36(a)] and reprinted with permission.)

Similar experiments were also conducted using polycrystalline W wire for the tip. The general features of the force gradient characteristics were the same as for the Ir tips: namely, negative interaction force gradients of the order of $10~\text{Nm}^{-1}$ were observed which increased rapidly in magnitude with decreasing tip-sample distance [35]. However, reproducibility of the experiments was poor if the tunnel resistance was below $\approx 1~\text{M}\Omega$. Under those conditions, the tunneling current exhibited violent fluctuations which were typically accompanied by a change of the atomic structure of the tip. The latter was checked by comparing tunneling images recorded before and after an approach experiment. Owing to these difficulties, the data are not complete enough to warrant a detailed analysis.

In the next step, Au and Al samples were investigated. The Al sample was made by evaporating a thin film (~200 nm) in situ onto an Ir-CB substrate at room

temperature. The Au samples were (111)-oriented thin films (~200 nm) epitaxially grown on a mica CB with mechanical properties similar to those of the Ir CB. Approach experiments were conducted in the same manner as described above, for which the tunnel resistance at the reference position was $10^7 \Omega$ and $10^8 \Omega$ for the Au and Al samples, respectively. The results of the force gradient measurements are shown in Figure 6(a), to which we have added the Ir result as a reference. Negative force gradients are also observed for the Au and Al samples at the beginning of the approach ramp, but the magnitude does not increase monotonically with decreasing gap width. Instead, a minimum is observed, and eventually the force gradient even becomes positive. The tunnel characteristics are exponential in the regime of negative interaction force gradients. Simultaneously with the force gradient becoming positive, the tunnel resistance curves level off as they

approach values of the order of $100~\mathrm{k}\Omega$. No apparent discontinuity in the tunnel resistance was observed in either case for tip excursions for which the force gradient was measured. Nevertheless, abrupt jumps in the tunnel conductivity were induced by further ramping the tip forward. However, the positions where these jumps occur, as well as the corresponding values of the tunnel resistance, were poorly reproducible.

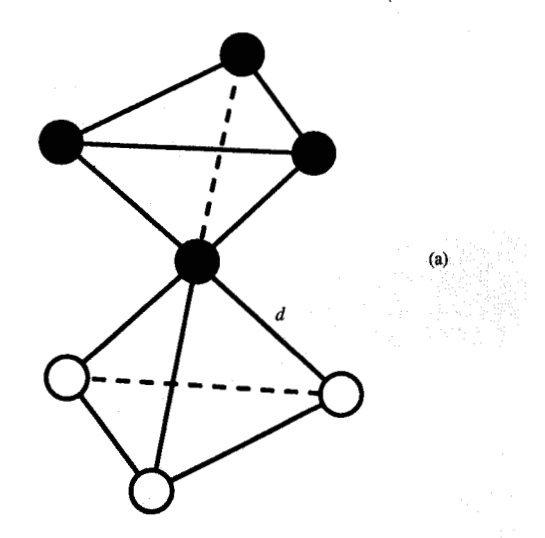
The force gradient characteristics for the Au and Al samples are clearly incompatible with Equation (17). We recall that in deriving this equation it was assumed that the adhesion properties of an atomic-sized asperity are the same as those of a macroscopic surface; i.e., we assumed that the many-body effects at the apex of the tip are similar to those at the macroscopic surface. On the other hand, one can adopt a different point of view [36] which focuses on localized electrons in contrast to the freeelectron picture of ideal metals. In the model calculation, the surface is represented by three layers of hexagonal symmetry with a total of 211 atoms. The tip consists of a base layer of 48 atoms, a second layer of 12 atoms, and a single atom on top of that. The total energy is calculated by summing nearest-neighbor two-body interactions. For this, one could use the interaction between two isolated atoms, calculated by a first-principles method. Summing such (pure) two-body interactions to obtain the energy of large systems would, however, ignore all many-body effects in metals. Therefore, effective nearest-neighbor interactions are determined by calculating small clusters consisting of seven atoms arranged in two parallel triangles with the seventh atom in between [Figure 7(a)]. To obtain the effective interaction energy between two like atoms, all distances d in the cluster are assumed to be the same, and the potential is defined as

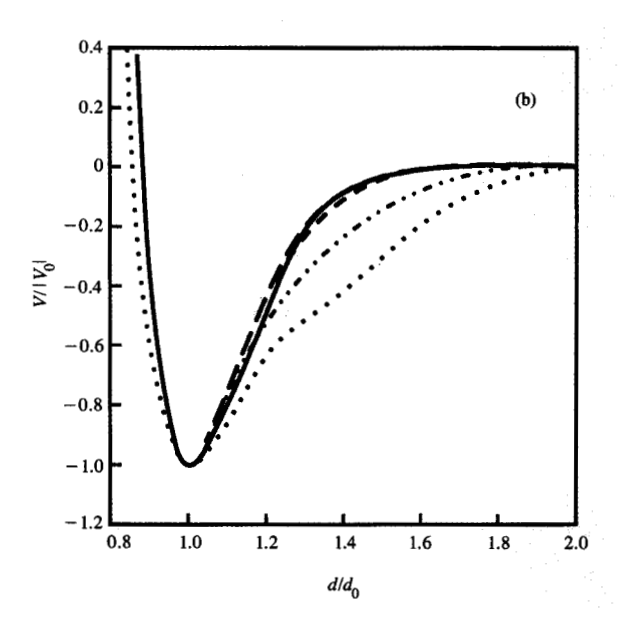
$$U_{m-m}(d) = \frac{1}{6} (E_7 - 2E_3 - E_1), \tag{20}$$

where E_n is the total energy of a cluster of n atoms. To obtain the effective two-body interaction between two different metals, a tetrahedral cluster of the first metal is taken to interact with a triangular cluster of the second metal at a distance d from the tip of the tetrahedron, and the potential is defined as

$$U_{m_1-m_2}(d) = \frac{1}{3} (E_7 - E_3^{(m_2)} - E_4^{(m_1)}), \tag{21}$$

where the bond lengths of the subclusters are adjusted to minimize the respective energies, thus producing their respective equilibrium geometries. The potentials in Equations (20) and (21) are calculated using a semiempirical tight-binding model with matrix elements calculated in an extended Hückel scheme. Effective potentials in Equations (20) and (21) are plotted in **Figure 7(b)**, where the energy V and the distance d are





(a) Cluster considered in the calculation of effective nearest-neighbor interactions. (b) Effective nearest-neighbor potentials scaled by the energy V_0 and distance d_0 at the potential minimum for

Ir-Ir with $V_0=-0.594$ eV, $d_0=0.268$ nm (solid line). Ir-Au with $V_0=-0.321$ eV, $d_0=0.284$ nm (long-dashed line). Au-Au with $V_0=-0.371$ eV, $d_0=0.28$ nm (short-dashed line). Ir-Al with $V_0=-0.377$ eV, $d_0=0.25$ nm (dashed-dotted line). Al-Al with $V_0=-0.258$ eV, $d_0=0.291$ nm (dotted line).

(Adapted from [36(a)] and reprinted with permission.)

rescaled by their respective values at the potential minimum. The Ir–Ir potential (solid line) and the Ir–Au potential (long-dashed line) fall off exponentially, with a decay constant slightly smaller than expected from

universality theory [23]. The decay constant of the Au-Au potential (short-dashed line) changes with distance. It is similar to that of the Ir-Au potential within 0.05 nm from the potential minimum but it increases slightly at larger separations, a fact that cannot be reconciled within the concept of universality. Deviations from universality are striking for the Al potentials (Ir-Al: dashed-dotted line, Al-Al: dotted line), which fall off much more slowly, with decay constants varying substantially with distance.

In the first set of calculations of the interaction energies and force gradients between an Ir tip and Ir, Au, and Al surfaces, the lattice spacings in the tip and the sample were kept at their equilibrium positions [see dashed curves in Figure 6(b)]. The width of the gap between tip and sample is defined here as the distance, Z, between the apex atom and the top atomic layer of the unrelaxed tip and sample, respectively. With this definition, experimental and calculated data can be readily compared. The experimental tip excursion scale z corresponds up to a constant offset to the gap width Z as defined in the calculations. As expected, the experimental data are well represented for the Ir surface. However, the calculated force gradient deviates significantly from the measured data for the Au and Al samples, being, in particular, one order of magnitude too large for the latter [right-hand scale in Figure 6(b)]. Good qualitative agreement with the Al data is achieved by replacing the Ir atom at the apex of the tip with an Al atom (dotted curve). It is conceivable that substrate atoms were picked up in the course of the experiment, because large sudden fluctuations in the tunneling current were frequently observed. Fluctuations also appear for the Au samples, so that we are also inclined to assume that the tip apex is formed by a Au atom (dotted curve), although the agreement with experiment is still rather poor. Note, however, that relaxation has been neglected thus far.

In the second calculation, the positions of the tip and sample atoms were allowed to relax in response to the interaction forces, keeping the base layers of each cluster fixed. Tip and sample surface relaxations are shown in Figure 6(c) as solid and dashed curves, respectively. Relaxation causes the average separation between the atom at the tip apex and its nearest atoms in the surface to decrease more rapidly than Z. Correspondingly, the force gradient curves also change, as shown by the solid curves in Figure 6(b). Relaxation effects are particularly pronounced for the Ir-Ir system. At the onset of making contact, the apex atom on the tip has moved toward the surface by as much as 0.05 nm, with a smaller upward motion of the surface atoms under the tip. Note that relaxation effects of that order of magnitude were also inferred from the analysis of experimental data.

For the Au-coated Ir tip approaching a Au surface, relaxation is smaller and less abrupt. This is somewhat

surprising at first, because Au is far less rigid than Ir. However, relaxation is determined by the interaction force gradients, which are smaller in this case because of the slower roll-off of the interaction potentials. With relaxation included, the calculated force gradient curve for the Aucoated tip is in good qualitative agreement with measured data. For the Al-coated Ir tip approaching an Al surface, much smaller force gradients are obtained as a consequence of the peculiarity of the Al-Al potential. Correspondingly, relaxation of the atomic positions is almost negligible, viz., less than one hundredth of a nanometer. Note that the outward motion of the apex and surface atoms is reversed when the force gradient is positive. This feature stabilizes the gap to a certain degree, which might explain why no jump to contact was observed in the experiment. One last point: The fact that relaxation is smallest for the Al sample might appear to contradict our conjecture of Al being picked up by the Ir tip. Note, however, that the force gradient for a clean Ir tip is always negative and assumes large values at short distances, making it very likely for Al to be ripped away from the surface.

Adhesion on the atomic scale is far more complex than expected on the basis of macroscopic adhesion theory. Whereas the Ir–Ir results can be consistently described within that framework, bimetallic contacts show distinct differences pointing at localized electronic (chemical) effects. As a further illustration for the complexity of tip–sample interactions, we show results obtained with a Pt–Ir alloy tip and a Ga(001) surface.

Preparation of the Ga(001) single-crystal surface is described in detail in [37]. Atomic-scale images revealed that the structure seen by the STM changes with the tunneling condition. For large values of the tunnel resistance $R_{\rm T} \gtrsim 10^8 \,\Omega$, viz., large tip-sample separation, the imaged structure [see Figure 8(a), left panel] is close to that of the truncated bulk (001) surface [37]. The apparent atomic configuration, however, is almost perfectly fcc [Figure 8(a), right panel] if the same surface is imaged at a tunnel resistance of less than $\approx 3 \times 10^7 \Omega$, viz., if the gap width is smaller.3 Evidently, the electron density distribution probed by the tip depends strongly on the tip-sample distance. It is highly unlikely that the lateral symmetry of the electron density distribution varies with distance on a metal surface in the absence of surface states or charge density waves. We have seen no spectroscopic indication of the existence of such states; hence, we think that this effect is due to a local distortion of the atomic lattice as a result of the tip-sample interaction.

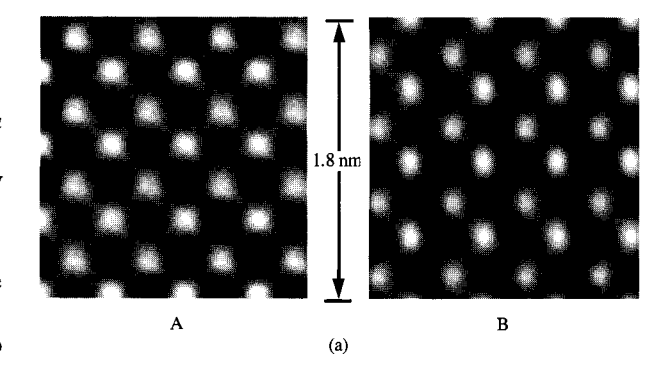
To corroborate this proposition, force gradient characteristics were measured. For this purpose the tip was mounted on a flexible CB and the sample stage was rigid. The tips were prepared from a thin Pt-Ir wire with

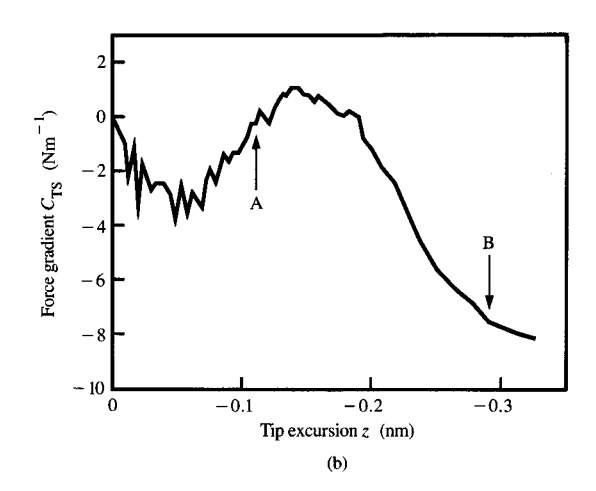
³ O. Züger and U. Dürig, work in preparation.

a diameter of 0.1 mm which was spot-welded onto a stainless steel CB. The apex of the tip was formed by cutting the wire at an angle of about 30 degrees with respect to the axis. Final tip forming was performed *in situ* in a similar fashion as for the Ir tips. However, the tipforming voltage could not be made larger than about 100 V because of Coulomb interaction, which for higher voltages was sufficiently strong to overcome the stiffness of the beam and thus force the tip to crash into the surface of the Ir test sample.

Experimental parameters and procedures were similar to those in the approach experiments described above. The data are displayed in Figure 8(b). At large tip-sample separations the force gradient is slightly negative, as expected for an attractive interaction. However, a local minimum followed by a distinct maximum is observed at tunnel resistances of 0.5 G Ω and 60 M Ω , respectively. As the gap width is further decreased, the interaction force gradient decreases monotonically until a second, deeper minimum is reached at a tunnel resistance of $\approx 10 \text{ M}\Omega$. The force gradient measurements thus prove two things: First, there is a substantial tip-sample interaction for the tunneling conditions used in imaging the Ga surface, and second, the interaction is qualitatively different for conditions A and B [see arrows in Figure 8(b)], which yield the surface structures resembling those of the truncated bulk and of an fcc lattice, respectively.

Bernasconi et al. [38] have shown by numerical calculation that the (001) surface of α -Ga is wetted by a bilayer of an epitaxial Ga(III) phase. Bulk Ga(III), stable at high pressure and temperature, crystallizes in a tetragonally distorted fcc lattice. When Ga(III) is forced to have the same in-plane lattice constants as those of α -Ga, the fcc-like symmetry is unstable, and the atoms align in a chain structure very similar to the one observed under condition A. This chain reconstruction is a subtle effect involving energy differences of the order of few tens of a meV per atom. Hence, it is conceivable that the requirement for reconstruction is locally relaxed by the presence of the tip. It seems, however, as though a slight barrier must be overcome in this process, which would explain the anomaly of the interaction force gradient at a tunnel resistance of $\approx 60 \text{ M}\Omega$. As the tip approaches the surface, the barrier collapses and an energetically more favorable configuration is established, as indicated by the rapidly decreasing force gradient. Most likely, one must visualize this process as a local distortion in which atoms are dragged or pushed around by the tip until they are trapped in positions which mimic the fcc-like structure. As the tip moves away, the displaced atoms snap back into the respective equilibrium positions of the free surface. This example demonstrates particularly clearly the importance of local atomic-scale interactions in scanning probe microscopies. Moreover, lattice distortions of this





(a) Atomic resolution images of the $\alpha\text{-}Ga(001)$ surface measured at a tunnel resistance of 100 $M\Omega$ (left panel) and 20 $M\Omega$ (right panel). (b) Force gradient characteristics for a Pt/Ir alloy tip above an $\alpha\text{-}Ga(001)$ surface. Tip–sample separations corresponding to a tunnel resistance of 100 $M\Omega$ and 20 $M\Omega$ are marked by arrows A and B, respectively.

kind must be associated with a dissipation of energy, which, in turn, gives rise to frictional forces, even though the tip and the sample do not make contact in the classical sense.

6. Force gradient mapping

Probing short-range interactions by means of force gradient sensing in combination with tunneling microscopy provides valuable additional information. Here, the STM is operated in the standard constant current mode, and the resonance frequency of the vibrating CB sample is measured simultaneously with the topography. Electron tunneling is determined by the overlap of wave functions of electrons at the Fermi level, $E_{\rm F}$. Hence, to the lowest order, the tunneling microscope probes the product of the state

densities at $E_{\rm F}$ of the tip and sample [39]. Interaction forces, on the other hand, involve all valence electrons and hence provide chemical information that is only marginally accessible by tunneling. A typical example of this is the contrast created by adsorbed atoms (or molecules) whose electronic states are shifted far from the Fermi level. Such atoms are almost invisible to the STM because the density of states at the Fermi level is almost the same as that of the bare substrate. The atoms simply act as part of the tip-substrate tunneling barrier. The situation is different for the interaction forces. Assuming that the atoms are covalently bound to the substrate, i.e., that all valence electrons are paired, the response of the bound atom to extra electrons is similar to that of closed-shell atoms. In other words, electrons are expelled, thus increasing their kinetic energy [40]. Therefore, one expects that such an adsorbed atom will give rise to a repulsive contribution to the total tip-sample interaction force.

In order to estimate the magnitude of the effect, additivity of the tip and substrate electron densities is assumed. This premise is reasonable for sufficiently large tip-substrate distances for which the tunnel resistance is greater than, say, $10 \text{ M}\Omega$. This means that if the tip is above the adsorbed atom, the latter is embedded in an electron cloud which also comprises those electrons from the tip that have leaked out over the tip adatom distance. The energy required for embedding a closed-shell atom in a free electron gas is of the order of 150 eV per unit electron density (in atomic units) [41]. The typical electron density within metals is of the order of 0.01-0.03. The density decays exponentially into vacuum with a characteristic length of $\kappa^{-1} \simeq 0.05$ nm. Hence, for the atom-induced repulsive tip-sample force, one obtains values of the order of (5-15 nN) $\times \exp(-\kappa s)$, and, correspondingly, for the force gradient $(100-300 \text{ Nm}^{-1}) \times \exp(-\kappa s)$. These values are comparable to those for the short-range adhesion interaction, but with opposite sign. Therefore, the adsorbed atoms should produce an easily detectable repulsive signal in the force gradient image. It is assumed in the above discussion that the adsorption of the adatom is effected by a pure covalent bond. In many instances, however, the nature of the binding is more complex and includes delocalized electrons and charge transfer. Under such conditions, the adatom-induced tip-sample interaction certainly comprises attractive dipole interactions as well as more complex embedding energies which need to be calculated by a first-principles method (see, e.g., [41]).

To demonstrate the principle of force gradient mapping, the same polycrystalline Ir sample was investigated that was used for measuring force gradient characteristics. From Auger analysis, it is shown that a residual contamination of carbon (notably the only contaminant detected) equivalent to a few percent of a monolayer

persisted even after several sputtering cycles. In addition, carbon coverage increased gradually at a rate of 0.2 monolayer per day when the sample was left in the UHV chamber. The oscillator method was used for measuring the resonance frequency of the CB simultaneously with the topography while raster-scanning the surface at a rate of one line per second. The detection bandwidth for the force gradient measurement was 100 Hz—compatible with the Nyquist criterion for 256 data points per line—which yields a force gradient sensitivity of $\approx 0.25 \text{ Nm}^{-1}$ (see the section on force sensing). The tunnel resistance was adjusted to 10 M Ω ($V_{\rm T}$ = 20 mV and $I_{\rm T}$ = 2 nA), a borderline value for detecting short-range adhesion forces but, on the other hand, one that provides a tunneling gap large enough to keep tip-induced modifications of the surface from being too severe (see below).

Two subsequently recorded images of the topography (displayed as a gradient image to enhance the visibility of small-scale features) and corresponding force gradient maps are displayed respectively in the left and right panels of **Figure 9(a)**. The gray scale in the force gradient maps is such that dark and light tones correspond to -8 Nm^{-1} and 0 Nm^{-1} , respectively. The most striking features in both maps are the dark and light spots with lateral dimensions of the order of 0.7 nm. These spots are henceforth also termed attractive and repulsive sites in accordance with the change of the tip-sample interaction toward stronger and weaker adhesion at the respective sites.

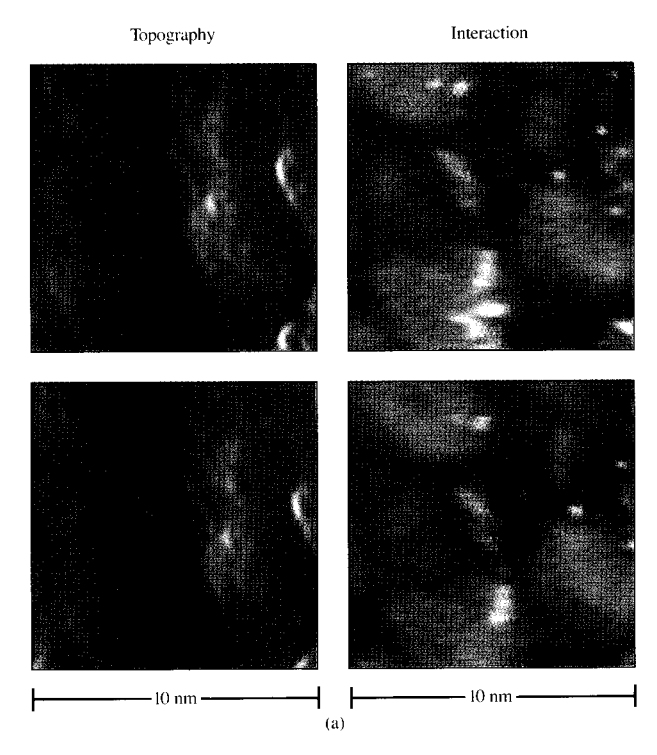
In comparing topography and force gradient images, one also recognizes that the tip-sample adhesion interaction is enhanced along trenches separating neighboring hillocks on the surface. The correlation between topographic and force gradient features is clearly visible in Figure 9(b), which is a three-dimensional rendering of the measured topography with the force gradient superimposed in color. The enhancement of the force gradient at the bottom of the grooves with respect to flat areas is typically around 50%. Respective values as large as 100% can be observed in extreme cases. An example of this is seen at the pronounced depression close to the center of the image. From these observations we conclude that the enhancement is produced mainly by geometry effects, i.e., by exposing the tip apex to a larger sample area while following V-shaped grooves. Geometry effects of that kind are expected to originate primarily from long-range vdW interactions which are always present in addition to shortrange forces.

The mechanism that gives rise to the light and dark spots, however, must be different from the geometry effects. We note that some of the bright spots (repulsive sites) visible on the upper force gradient map are absent in the subsequently recorded lower map. In fact, repetitive scanning of the same area had a "cleansing" effect. With the exception of some spots coinciding with pronounced

topographic grooves, all repulsive sites had disappeared by the end of the fifth scan. On the basis of Auger analysis, the repulsive sites are identified as adsorbed carbon atoms (or clusters thereof). This conjecture is corroborated by complementary observations. Consistent with the Auger results, the density of the repulsive sites is substantially higher for samples that had been left in the chamber for an extended period. In addition, lateral dimensions of the spots are in agreement with the size of carbon atoms observed by STM [42]. Finally, it is not surprising that adsorbed carbon atoms are relatively easily removed by the scanning motion of the tip. The bond of atomic carbon with Ir is not very strong because larger monolayer clusters spontaneously transform into graphite overlayers rather than remaining in the carbidic form [43]. The origin of the dark spots is less clear. These attractive sites were about one order of magnitude less abundant than the repulsive ones. Most likely, they also arise from adsorbed atoms, because no topographic features could be detected at these sites that would indicate geometry-induced effects.

This example clearly demonstrates the power of combining interaction force detection and standard tunneling microscopy. The tunneling current is only marginally sensitive to the adsorbed carbon atoms. A detailed analysis of the data reveals that the repulsive sites give rise to a topographic contrast of 0.03 nm [29]. For such features to be detectable by STM alone, the topography of the substrate surface would have to be known with comparable accuracy a priori. This is definitely very difficult to achieve for rough surfaces with a broad distribution of corrugation amplitudes. Even by comparing the subsequently recorded topographic maps, it is extremely difficult to discern the places where adsorbed carbon atoms had been removed. The interaction force gradient, however, provides a clearly detectable flag which facilitates identification.

As a further example, the oxidation of polycrystalline Al films was investigated. Samples were prepared in the same way as for the force gradient characteristics measurements. The film was then exposed in situ to a dose of one monolayer equivalent of oxygen. Simultaneous STM and force gradient measurements were performed immediately thereafter. A perspective view of a 40×40 nm² section of the sample is shown in Figure 10. The force gradient data are superimposed in color, with green and yellow tones corresponding to negative ($\approx -5 \text{ Nm}^{-1}$) and positive ($\approx +30 \text{ Nm}^{-1}$) values, respectively. The dark areas in the figure are artifacts produced by spikes in the tunneling current which disturbed the proper operation of the frequency measuring electronics. The image was recorded using a bias voltage of 100 mV and a current of 1 nA. Under such conditions, a negative tip-sample force gradient of the order of 3-5 Nm⁻¹ is measured on freshly prepared Al surfaces (see the section on force gradient



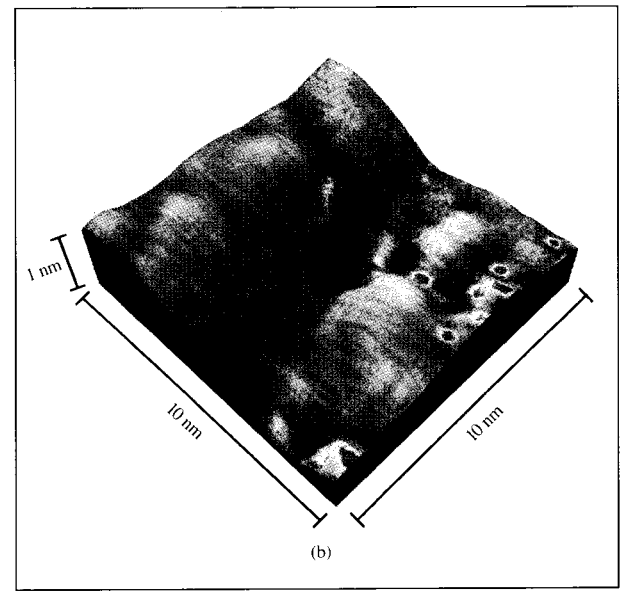


Figure 9

(a) Topography (left panels, displayed as gradient images to enhance visibility of small-scale features) and force gradient maps (right panels, dark and light tones corresponding to $-8~\mathrm{Nm}^{-1}$ and $0~\mathrm{Nm}^{-1}$, respectively) of a $10~\mathrm{X}$ 10-nm area of a sputter-cleaned Ir surface. Two sets of subsequently recorded data are displayed in the upper and lower panels, respectively. Bright spots on the force gradient maps can be identified as adsorbed carbon atoms which produce only negligible contrast in the topographic images. Tunneling conditions were $I_{\mathrm{T}} = 2~\mathrm{nA}, V_{\mathrm{T}} = -20~\mathrm{mV}$. (b) Three-dimensional rendering of the topography with the force gradient superimposed in color (dark brown = $-8~\mathrm{Nm}^{-1}$ and green = $0~\mathrm{Nm}^{-1}$ of the data displayed in the upper panels in (a).

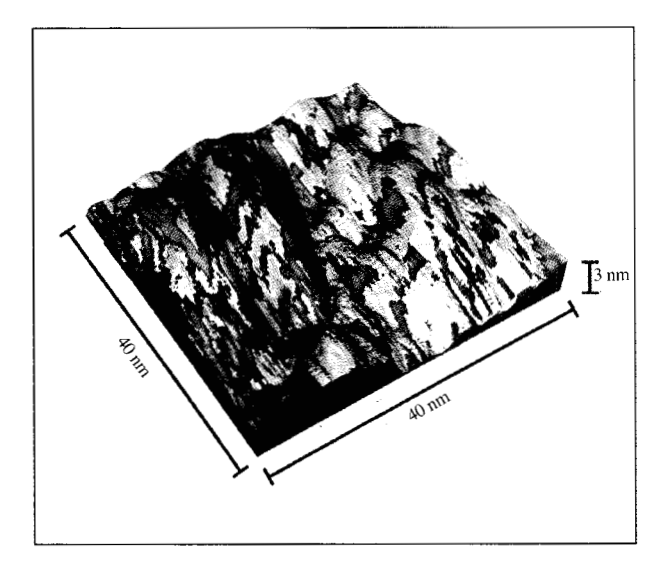


Figure 10

Perspective view of the topography of a condensed Al film exposed to one-monolayer equivalent of oxygen with the interaction force gradient superimposed in green, $-5~{\rm Nm}^{-1}$, and yellow, $+30~{\rm Nm}^{-1}$, tones (dark colors are artifacts produced by noise in the tunneling current). Yellow areas can be identified as oxidized Al. Tunnel conditions were $I_{\rm T}=1~{\rm nA}$, $V_{\rm T}=-100~{\rm mV}$. (Adapted from [29] and reprinted with permission.)

characteristics). Hence, green areas in Figure 10 are identified as nonoxidized regions, whereas yellow areas indicate oxide, which gives rise to a nonmetallic repulsive tip—sample interaction. The oxidation of the polycrystalline Al film proceeds nonuniformly. It was found that after exposure to a higher dose (equivalent to five monolayers of oxygen), a few clean areas were still present. At the same time, tunneling became increasingly difficult on some of the repulsive areas, indicating a substantial vertical growth of the oxide layer. Note also that in this example the distinction of the chemical state of the surface was made possible only by the additional force gradient information.

7. Conclusions

U. DÜRIG

The interaction between a sharply pointed metal tip and a flat metallic sample has been investigated on the basis of known theory of long-range vdW and short-range adhesion forces. The short-range interaction is essentially determined by the atomic structure of the very apex of the tip irrespective of the tip-sample separation. VdW forces, in contrast, probe a much larger area of the tip, and are consequently insensitive to atomic-scale details. In fact, the tip shape expressed in terms of the cross section is averaged on a scale comparable to the distance from the sample. Although the adhesion energy per unit area due to the vdW interaction is about one order of magnitude

weaker than that due to the short-range interaction, the vdW interaction still contributes substantially to the tip-sample force even at distances close to contact. However, the vdW contribution changes only little with distance; hence, it is almost completely suppressed in the interaction force gradient. The latter can easily be determined by measuring the resonance frequency of a spring to which either the tip or the sample is attached. This technique has been used for studying the metallic adhesion interaction of Ir tips and Ir, Au, and Al samples. The results obtained for the Ir sample are well described within the framework of universal bulk adhesion theory. Qualitative differences were found for the Au and Al samples, however. These differences can be understood to arise from deviations from universality in the effective nearest-neighbor interaction and from the relaxation of the lattice as the tip approaches the surface. Complex adhesion behavior was observed in experiments performed on the (001) surface of α -Ga. Here, the tip-sample interaction induces a substantial local distortion of the atomic lattice at the surface. Furthermore, the interaction force gradient characteristics hint at the existence of a slightly repulsive barrier. This barrier separates a metastable configuration of the Ga surface that is observed at short tip-sample distances from the stable configuration of the free surface. Short-range forces are sensitive to the chemical state of the sample surface. This property is exploited in force gradient mapping. For this purpose the STM is operated in the constant current imaging mode, and the topography and shifts of the resonance frequency of the force sensor are recorded simultaneously. It is shown that the force gradient contrast created by adsorbed carbon and oxidation provides a clear flag for their detection even if the substrate surface is rough.

Acknowledgments

It was a pleasure to collaborate extensively with O. Züger, who performed thorough STM studies of the Ga surface as part of his Ph.D. thesis and who made in aluable contributions to this work in many ways. I also thank H. J. Kreuzer for his theoretical work, which led to a better understanding of tip-sample interaction effects, and A. Baratoff and S. Ciraci for many fruitful discussions. Finally, I also thank U. Maier for invaluable technical assistance and B. Michel for making the Au samples.

References

- B. V. Derjaguin, A. S. Titijevskaja, I. I. Abricossova, and A. D. Malkina, "Investigations of the Forces of Interaction of Surfaces in Different Media and Their Application to the Problem of Colloid Stability," Disc. Faraday Soc. 18, 24 (1954).
- D. Tabor and R. H. S. Winterton, "Surface Forces: Direct Measurement of Normal and Retarded van der Waals Forces," Nature 219, 1120 (1968); D. Tabor and R. H. S. Winterton, "The Direct Measurement of Normal and

- Retarded van der Waals Forces," Proc. Roy. Soc. A 312, 106 (1969).
- J. N. Israelachvili and D. Tabor, "Measurement of van der Waals Dispersion Forces in the Range 1.4 to 130 nm," Nature 236, 106 (1972); J. N. Israelachvili and D. Tabor, "The Measurement of van der Waals Dispersion Forces in the Range 1.5 to 130 nm," Proc. Roy. Soc. A 331, 19 (1972).
- J. N. Israelachvili and M. D. Pashley, "Molecular Layering of Water at Surfaces and Origin of Repulsive Hydration Forces," *Nature* 306, 204 (1983); H. K. Christenson and R. G. Horn, "Solvation Forces Measured in Non-Aqueous Liquids," *Chem. Scripta* 25, 37 (1985).
- For an overview of the subject, see e.g. J. N. Israelachvili, *Intermolecular and Surface Forces*, second edition, Academic Press, London, 1991.
- B. V. Derjaguin, Y. I. Rabinovich, and N. V. Churaev, "Measurement of Forces of Molecular Attraction of Crossed Fibres as a Function of Width of Air Gap," Nature 265, 520 (1977).
- D. H. Buckley, "The Metal-to-Metal Interface and Its Effects on Adhesion and Friction," J. Colloid Interface Sci. 58, 36 (1977).
- S. K. Roy Chowdhury and H. M. Pollock, "Adhesion Between Metal Surfaces: The Effect of Surface Roughness," Wear 66, 307 (1981); M. D. Pashley, J. B. Pethica, and D. Tabor, "Adhesion and Micromechanical Properties of Metal Surfaces," Wear 100, 7 (1984); M. D. Pashley and J. B. Pethica, "The Role of Surface Forces in Meta-Metal Contacts," J. Vac. Sci. Technol. A 3, 757 (1985).
- See e.g. D. Maugis and H. M. Pollock, "Surface Forces, Deformation and Adherence at Metal Microcontacts," Acta Metall. 32, 1323 (1984).
- For a review, see e.g. Scanning Tunneling Microscopy: Theory and Application, D. Bonell, Ed., VCH Publishers, Weinheim, 1993; D. Sarid, Scanning Force Microscopy with Applications to Electric, Magnetic, and Atomic Forces, Oxford Series in Optical Sciences, M. Lapp and H. Stark, Eds., Oxford University Press, Oxford, U.K., 1991.
- C. M. Mate, G. M. McClelland, R. Erlandsson, and S. Chiang, "Atomic-Scale Friction of a Tungsten Tip on a Graphite Surface," *Phys. Rev. Lett.* 59, 1942 (1987); O. Marti, J. Colchero, and J. Mlynek, "Combined Scanning Force and Friction Microscopy of Mica," *Nanotechnol.* 1, 141 (1990); G. Meyer and N. M. Amer, "Simultaneous Measurement of Lateral and Normal Forces with an Optical-Beam-Deflection Atomic Force Microscope," *Appl. Phys. Lett.* 57, 2089 (1990).
- For reviews, see Fundamentals of Friction: Macroscopic and Microscopic Processes, I. L. Singer and H. M. Pollock, Eds., NATO ASI Series E: Applied Sciences, Vol. 220, Kluwer, Dordrecht, 1992; E. Meyer, R. M. Overney, and J. Frommer, "Lubrication Studied by Friction Force Microscopy," to be published in Textbook of Microtribology, CRC Press, Inc., Boca Raton, FL, 1994
- 13. N. A. Burnham and R. J. Colton, "Measuring the Nanomechanical Properties and Surface Forces of Materials Using an Atomic Force Microscope," J. Vac. Sci. Technol. A 7, 2906 (1989); G. S. Blackman, C. M. Mate, and M. R. Philpott, "Interaction Forces of a Sharp Tungsten Tip with Molecular Films on Silicon Surfaces," Phys. Rev. Lett. 65, 2270 (1990); S. R. Cohen, G. Neubauer, and G. M. McClelland, "Nanomechanics of a Au-Ir Contact Using a Bidirectional Atomic Force Microscope," J. Vac. Sci. Technol. A 8, 3449 (1990); A. L. Weisenhorn, P. Maivald, H.-J. Butt, and P. K. Hansma, "Measuring Adhesion, Attraction, and Repulsion Between Surfaces in Liquids with an Atomic Force

- Microscope," Phys. Rev. B 45, 11226 (1992).
- 14. U. Landman, W. D. Luedtke, N. A. Burnham, and R. J. Colton, "Atomistic Mechanisms and Dynamics of Adhesion, Nanoindentation and Fracture," Science 248, 454 (1990); J. A. Harrison, C. T. White, R. J. Colton, and D. W. Brenner, "Nanoscale Investigation of Indentation, Adhesion and Fracture," Surf. Sci. 271, 57 (1992); T. N. Todorov and A. P. Sutton, "Jumps in Electronic Conductance Due to Mechanical Instabilities," Phys. Rev. Lett. 70, 2138 (1993).
- For a recent review, see F. Grey, "STM-Based Nanotechnology: The Japanese Challenge," Adv. Mater. 5, 704 (1993).
- U. Dürig, J. K. Gimzewski, and D. W. Pohl, "Experimental Observation of Forces Acting During Scanning Tunneling Microscopy," *Phys. Rev. Lett.* 57, 2403 (1986).
- E. M. Lifshitz, "The Theory of Molecular Attractive Forces Between Solids," Sov. Phys. JETP 2, 73 (1956).
- 18. H. Krupp, "Particle Adhesion: Theory and Experiment," Adv. Colloid Interface Sci. 1, 139 (1967).
- J. Heinrichs, "Non-Local Effects in the Macroscopic Theory of van der Waals and Adhesive Forces," Solid State Commun. 13, 1595 (1973); J. E. Inglesfield and E. Wikborg, "The van der Waals Interaction Between Metals," J. Phys. F: Metal Phys. 5, 1475 (1975).
 J. E. Inglesfield, "Adhesion Between Al Slabs and
- J. E. Inglesfield, "Adhesion Between Al Slabs and Mechanical Properties," J. Phys. F: Metal Phys. 6, 687 (1976)
- J. Ferrante and J. R. Smith, "A Theory of Adhesion at a Bimetallic Interface: Overlap Effects," Surf. Sci. 38, 77 (1973); A. V. Kobelev, R. M. Kobeleva, and V. F. Ukhov, "On the Adhesion Theory of Two Metallic Surfaces," Phys. Status Solidi B 96, 169 (1979); M. P. Das and N. Nafari, "A Model for Bimetallic Interfaces," Solid State Commun. 58, 29 (1986).
- J. Vannimenus and H. F. Budd, "Selfconsistent Calculation of Forces Between Two Metallic Half Spaces," Solid State Commun. 17, 1291 (1975).
- J. H. Rose, J. Ferrante, and J. R. Smith, "Universal Binding Curves for Metals and Bimetallic Interfaces," *Phys. Rev. Lett.* 47, 675 (1981); *idem*, "Theory of the Bimetallic Interface," *Phys. Rev. B* 31, 3427 (1985).
 S. Ciraci, A. Baratoff, and I. P. Batra, "Tip-Sample
- 24. S. Ciraci, A. Baratoff, and I. P. Batra, "Tip-Sample Interaction Effects in Scanning Tunneling and Atomic-Force Microscopy," *Phys. Rev. B* 41, 2763 (1990); *idem*, "Site-Dependent Electronic Effects, Forces, and Deformations in Scanning Tunneling Microscopy on Flat Metal Surfaces," *Phys. Rev. B* 42, 7618 (1990).
- J. H. Rose, J. R. Smith, and J. Ferrante, "Universal Features of Bonding in Metals," Phys. Rev. B 28, 1835 (1983)
- H.-W. Fink, "Mono-Atomic Tips for Scanning Tunneling Microscopy," IBM J. Res. Develop. 30, 460 (1986).
- N. A. Burnham, R. J. Colton, and H. M. Pollock, "Work Function Anisotropies as an Origin of Long-Range Surface Forces," *Phys. Rev. Lett.* 69, 144 (1992); J. E. Inglesfield, "Comment on Work Function Anisotropies as an Origin of Long-Range Surface Forces," *Phys. Rev. Lett.* 70, 246 (1993)
- 28. For a review, see e.g. P. Grütter, H. J. Mamin, and D. Rugar, "Magnetic Force Microscopy," Springer Series in Surface Science 28, 151 (1992).
- U. Dürig, O. Züger, and A. Stalder, "Interaction Force Detection in Scanning Probe Microscopy: Methods and Applications," J. Appl. Phys. 72, 1778 (1992).
- 30. A similar scheme was developed independently by T. R. Albrecht, P. Grütter, D. Horne, and D. Rugar, "Frequency Modulation Detection Using High-Q Cantilevers for Enhanced Force Microscopy Sensitivity," J. Appl. Phys. 69, 668 (1991).

- A. Banerjea, J. R. Smith, and J. Ferrante, "Universal Aspects of Adhesion and Atomic Force Microscopy," J. Phys.: Condens. Matter 2, 8841 (1990).
- U. Dürig, O. Züger, and D. W. Pohl, "Observation of Metallic Adhesion Using the Scanning Tunneling Microscope," Phys. Rev. Lett. 65, 349 (1990).
- 33. W. R. Tyson and W. A. Miller, "Surface Free Energies of Solid Metals: Estimation from Liquid Surface Tension Measurements," *Surf. Sci.* **62**, 267 (1977).
- J. K. Gimzewski and R. Möller, "Transition from the Tunneling Regime to Point Contact Studied Using Scanning Tunneling Microscopy," Phys. Rev. B 36, 1284 (1987).
- U. Dürig, O. Züger, B. Michel, L. Häussling, and H. Ringsdorf, "Electronic and Mechanical Characterization of Self-Assembled Alkanethiol Monolayers by Scanning Tunneling Microscopy Combined with Interaction-Force-Gradient Sensing," Phys. Rev. B 48, 1711 (1993).
 (a) U. Dürig, O. Züger, L. C. Wang, and H. J. Kreuzer,
- (a) U. Dürig, O. Züger, L. C. Wang, and H. J. Kreuzer, "Adhesion in Atomic-Scale Metal Contacts," *Europhys. Lett.* 23, 147 (1993);
 (b) L. C. Wang and H. J. Kreuzer, private communication.
- O. Züger and U. Dürig, "Atomic Structure of the α-Ga(001) Surface Investigated by Scanning Tunneling Microscopy: Direct Evidence for the Existence of Ga₂ Molecules in Solid Gallium," Phys. Rev. B 46, 7319 (1992).
- M. Bernasconi, G. L. Chiarotti, and E. Tosatti, "The (001) Surface of α-Ga Is Covered with GaIII," *Phys. Rev. Lett.* 70, 3295 (1993).
- J. Tersoff and D. R. Hamann, "Theory and Application for the Scanning Tunneling Microscope," Phys. Rev. Lett. 50, 1998 (1983); A. Baratoff, "Theory of Scanning Tunneling Microscopy—Methods and Approximations," Physica 172B, 143 (1984); N. D. Lang, "Theory of Single-Atom Imaging in the Scanning Tunneling Microscope," Phys. Rev. Lett. 56, 1164 (1986).
- 40. G. G. Kleinman and U. Landman, "Theory of Physisorption: He on Metals," *Phys. Rev. B* 8, 5484 (1973)
- 41. S. Holloway and J. K. Nørskov, "The Binding of Adsorbates to Metal Surfaces," *Springer Series in Surface Science* 2, 18 (1984).
- 42. H. Brune, J. Wintterlin, G. Ertl, and R. J. Behm, "Direct Imaging of Adsorption Sites and Local Electronic Bond Effects on a Metal Surface: C/Al(111)," Europhys. Lett. 13, 123 (1990).
- 43. N. A. Kholin, E. V. Rut'kov, and A. Y. Tontegode, "The Nature of the Adsorption Bond Between Graphite Islands and Iridium Surface," Surf. Sci. 139, 155 (1984).

Received February 15, 1994; accepted for publication May 9, 1994

Urs Dürig IBM Research Division, Zurich Research Laboratory, Säumerstrasse 4, 8803 Rüschlikon, Switzerland (DRG at ZURICH). Dr. Dürig received his Diploma in experimental physics and his Ph.D. degree from the Swiss Federal Institute of Technology (ETH), Zurich, in 1979 and 1984, respectively. He then spent a postdoctoral fellowship at the IBM Research Laboratory in Rüschlikon working on nearfield optical microscopy in the group of D. W. Pohl, and became a Research Staff Member in 1986. Since then, he has been studying surface properties of metals using the scanning tunneling microscope and related local probe techniques.